Published in final edited form as:
Phys Med Biol. 2009 November 7; 54(21): 6495. doi:10.1088/0031-9155/54/21/004.

Timing resolution of scintillation-detector systems: a Monte Carlo analysis

Woon-Seng Choong
Department of Radiotracer Development and Imaging Technology, Lawrence Berkeley National Laboratory, 1 Cyclotron Road, Mailstop 55R0121, Berkeley, CA 94720, USA

Abstract

Recent advancements in fast scintillating materials and fast photomultiplier tubes (PMTs) have stimulated renewed interest in time-of-flight (TOF) positron emission tomography (PET). It is well known that the improvement in the timing resolution in PET can significantly reduce the noise variance in the reconstructed image resulting in improved image quality. In order to evaluate the timing performance of scintillation detectors used in TOF PET, we use a Monte Carlo analysis to model the physical processes (crystal geometry, crystal surface finish, scintillator rise time, scintillator decay time, photoelectron yield, PMT transit time spread, PMT single-electron response, amplifier response, and time pick-off method) that can contribute to the timing resolution of scintillation-detector systems. In the Monte Carlo analysis, the photoelectron emissions are modeled by a rate function, which is used to generate the photoelectron time points. The rate function, which is simulated using Geant4, represents the combined intrinsic light emissions of the scintillator and the subsequent light transport through the crystal. The PMT output signal is determined by the superposition of the PMT single-electron response resulting from the photoelectron emissions. The transit time spread and the single-electron gain variation of the PMT are modeled in the analysis. Three practical time pick-off methods are considered in the analysis. Statistically, the best timing resolution is achieved with the first photoelectron timing. The calculated timing resolution suggests that a leading edge discriminator gives better timing performance than a constant fraction discriminator and produces comparable results when a 2-threshold or 3-threshold discriminator is used. For a typical PMT, the effect of detector noise on the timing resolution is negligible. The calculated timing resolution is found to improve with increasing mean photoelectron yield, decreasing scintillator decay time, and decreasing transit time spread. However, only substantial improvement in the timing resolution is obtained with improved transit time spread if the first photoelectron timing is less than the transit time spread. While the calculated timing performance does not seem to be affected by the pixel size of the crystal, it improves for an etched crystal compared to a polished crystal. In addition, the calculated timing resolution degrades with increasing crystal length. These observations can be explained by studying the initial photoelectron rate. Experimental measurements provide reasonably good agreement with the calculated timing resolution. The Monte Carlo analysis developed in this work will allow us to optimize the scintillation detectors for timing and to understand the physical factors limiting their performance.

wschoong@lbl.gov.

1. Introduction

Recently, there has been a renewed interest in time-of-flight (TOF) positron emission tomography (PET) (Moses 2003 and Muehllehner *et al* 2006) due to the advancements in new scintillation materials, detector technologies, and readout electronics. It is well known that the improvement in the coincidence timing resolution in PET can significantly improve the signal-to-noise ratio (SNR) in the reconstructed image (Campagnolo *et al* 1979, Snyder *et al* 1981, Tomitani 1981, Harrison *et al* 2004, Conti 2006 and Surti *et al* 2006). In conventional PET, the location of an individual positron is determined after it decays to form a pair of back-to-back 511 keV photons, which subsequently interact in a pair of scintillation detectors placed opposite to each other. Because there is no time-of-flight (TOF) information in conventional PET, the positions of the positron annihilation are then known to lie on a line joining the two interaction positions. In principle, if we could accurately measure the difference in arrival time of the two annihilation photons, then the position of the positron would be constrained to a point rather than a line; so three-dimensional images could be obtained without a reconstruction algorithm. However, the position along the line is localized to $\Delta x = (c/2)\Delta t$ where Δx is the position error, c is the speed of light, and Δt is the error in the timing measurement. Timing resolution of a few hundred picoseconds only constrains the positron position to a few centimeters. While this does not improve the spatial resolution, it has been shown to reduce the statistical noise in the reconstructed image if the line segment was shorter than the size of the emission source (Campagnolo *et al* 1979, Snyder *et al* 1981 and Tomitani 1981). This multiplicative reduction factor f (corresponding to the reduction in noise variance) is given by $f = D / \Delta x$ where D is the size of the emission source. Equivalently, as signal-to-noise ratio is proportional to the square root of counts, the improvement in SNR can therefore be estimated by $SNR_{TOF} = \sqrt{f} \bullet SNR_{conv}$ where SNR_{TOF} is the SNR in the TOF image and SNR_{conv} is the SNR in the conventional image. Therefore, it is important to know the fundamental limit of the timing resolution of a practical scintillation-detector system. More importantly, it is also very useful to understand how the physical processes of the individual basic components of a scintillation-detector system affect its timing performance. This information can be used to optimize the timing resolution of scintillation-detector systems developed for TOF PET.

The basic components of a scintillation-detector system are the scintillation crystal, the photomultiplier tube (PMT), and the readout electronics. Fast scintillators such as cerium-doped lutetium orthosilicate (LSO) (Melcher and Schweitzer 1992) and lanthanum bromide ($LaBr_3$) (van Loef *et al* 2002) are being used to develop TOF PET cameras. Fast PMTs with fewer multiplying stages and higher quantum efficiency (QE), or PMTs employing a microchannel plate (MCP) (Va'vra *et al* 2007), are being utilized to achieve better timing resolution. In addition to the scintillating material and PMT, there are a number of physical processes that can affect the timing performance, which include the crystal geometry, the crystal surface finish, the reflecting material, the front-end amplifier, and the time pick-off electronics.

Optimal timing estimators and Monte Carlo analyses have been developed to calculate the timing performance of scintillation detectors. While all these analyses have accurately considered the statistic of the photon detection, none have included all the physical processes in a practical scintillation-detector system in their calculation. Some have ignored the timing properties of the PMT (Post and Schiff 1950). While others have included the timing properties of the PMT, they simplified the photoelectron emission by assuming either a single exponential (Lynch 1966 and Tomitani 1982) or a bi-exponential (Hyman 1965, Clinthorne *et al* 1990 and Binkley 1994) model. A single exponential has been used to represent the scintillator decay time due to the radiative recombination. An exponential rise was added to represent the combined scintillator rise time due to the energy transfer to the luminescence centers and the

rate of the scintillation photons exiting the crystal. While attempts have been made to include an additional time variance in Hyman theory to describe the time spread in the scintillator (Bengtson *et al* 1970), they do not accurately represent the complex process when the scintillation photons generated at a point in the crystal have to undergo multiple reflections and different propagation time delays before exiting the crystals to be detected by the PMT. In addition, the propagation dispersion of the photons contributes to the initial rate of the photoelectron emission, which is a critical component in determining the timing of the scintillation detector, and cannot be accurately modeled by just an exponential rise. Furthermore, most of these analyses were performed for slow scintillators (Clinthorne *et al* 1990 and Binkley 1994) and do not represent the faster scintillators such as LSO and $LaBr_3$.

The objective of this work is to develop a Monte Carlo analysis to calculate the timing performance of a practical scintillation-detector system that includes all possible physical processes, notably the intrinsic scintillation photons generation, the propagation of the photons inside the crystal, the timing properties of the PMT, and the time pick-off methods. In this analysis we evaluate the individual physical factors (crystal geometry, crystal surface finish, scintillator rise time, scintillator decay time, photoelectron yield, PMT transit time spread, PMT single-electron response, amplifier response, and time pick-off method) that can affect the timing resolution of a scintillation-detector system. Some of the calculated results are compared with experimental measurements to validate the accuracy of the Monte Carlo analysis.

2. Materials and methods

2.1. Monte Carlo analysis of timing performance

The Monte Carlo analysis models a scintillation detector as shown in Figure 1, which is comprised of a scintillator crystal coupled on one side to the input window of the PMT (the crystal used in PET is normally long and narrow, and the narrow side is coupled to the PMT). Reflecting materials are applied to all sides of the crystal except the side coupled to the PMT. Crystals with different surface finishes, lengths and pixel sizes are simulated.

Figure 2 shows a block diagram describing the Monte Carlo timing analysis. It starts with a known normalized rate function, which represents the mean photoelectron emission rate at the photocathode of the PMT. By separating the scintillator response as an independent rate function, the timing analysis can be performed for any detector system as long as the rate function is known. Modeling of the scintillator response is described in section 2.3. It is known that a Poisson process describes the photoelectron emission. Because the rate function is time dependent, an inhomogeneous Poisson process is used to generate the individual photoelectron time points. The output signal of the PMT is a convolution of the generated photoelectrons with the single-electron response (SER) of the PMT. The statistical variation of the SER is modeled by the transit time spread and the SER gain distribution as described in section 2.2. Detector noise is modeled as a Gaussian distribution and is added to the output signal. However, all the simulations are performed without any detector noise except when studying the effect of the timing resolution on the noise. For each Monte Carlo realization, the simulated timing spectrum of a single detector is determined by applying a time pick-off method (as discussed in section 2.4) to 100,000 generated output signals. All the results in the timing analysis are for a single-detector timing resolution. The coincidence timing resolution is approximately $\sqrt{2}$ times the single-detector timing resolution.

2.2. PMT single-electron response

The SER of the PMT used in the Monte Carlo timing analysis closely models the measured SER of a fast PMT (Hamamatsu R-9800). The SER of the PMT is measured by exciting the

PMT with a pulsed laser diode driven by the Hamamatsu Picosecond Light Pulser (PLP-01). The laser pulse has an emission wavelength of 650 nm and is attenuated with enough neutral density filters so that the average number of photoelectrons per pulse is less than 1. The mean SER of the PMT is measured and digitized with a 1 GHz bandwidth oscilloscope terminated into a 51 Ω load (Tektronix TDS 684B). The amplitude of the SER is also recorded to obtain a normalized SER gain distribution. The mean SER can be fitted reasonably well with a *CR*–$(RC)^4$ Gaussian model (Knoll 2000) as shown in Figure 3:

$$V \propto \frac{t}{\tau} e^{-t/\tau} \tag{1}$$

The peaking time of SER pulse is given by 4τ. In the Monte Carlo timing analysis, we evaluate the dependence of the timing resolution on the width of the SER by setting τ = 0.07, 0.12, 0.20, or 0.27 ns (0.27 represents the measured SER of R-9800 PMT), which corresponds to a full width at half maximum (FWHM) of the pulse T_W = 0.31, 0.53, 0.88, or 1.18 ns respectively. The measured single-electron gain distribution is shown in Figure 4, which is modeled as a truncated Gaussian function having a resolution of 85% FWHM.

The transit time spread, TTS, of a PMT is obtained with a coincidence timing measurement. Both the trigger output of the PLP-01 controller and the PMT signal are read out with a constant fraction discriminator module (Canberra 454 NIM CFD). The outputs of the CFD are sent to a time-to-digital converter (Ortec 556 NIM TAC). The measured coincidence timing spectrum is shown in Figure 5, which is modeled by a Gaussian function having a timing resolution of 261 ps FWHM. In the Monte Carlo timing analysis, we evaluate the dependence of the timing resolution on the transit time spread by setting TTS = 100, 200, 300, or 400 ps FWHM.

2.3. Modeling scintillator response

The modeling of the scintillator response includes the generation of the scintillation photons inside the crystal and the subsequent tracking of the individual photon until it exits the crystal to be detected by the PMT. The simulated scintillation material is LSO, which has an index of refraction of 1.82, an emission wavelength of 420 nm, and a photon absorption length of 20 cm. The crystal is a rectangular box with a long and a narrow side. The narrow side is a square pixel with dimensions 4 mm × 4 mm or 6 mm × 6 mm. For each pixel size, four crystal lengths are considered: 10 mm, 15 mm, 20 mm, or 25 mm. All sides of the crystal are wrapped with a reflecting material except the side that couples to the PMT. The result of simulating the scintillator response is a photoelectron rate distribution normalized to the mean photoelectron yield that is used as the input to the Monte Carlo timing analysis as discussed in section 2.1. Figure 6 shows the result of the scintillator response for a 6 mm × 6 mm × 20 mm LSO crystal. Clearly, the leading edge of the photoelectron rate is more complicated than just an exponential rise.

2.3.1. Intrinsic photon generation—When the gamma ray enters the crystal and deposits its energy at the interaction point, scintillation photons are generated. The depth of the generated photons from the entrance follows an exponential distribution given by the interaction length of a 511 keV gamma ray in LSO, which is 12 mm. The scintillation photons are generated using an inhomogeneous Poisson process following an intrinsic intensity $I(t)$ described by a bi-exponential model:

$$I(t) = \frac{I_0}{\tau_d - \tau_r}\left[e^{-t/\tau_d} - e^{-t/\tau_r}\right] \tag{2}$$

where τ_r and τ_d are the intrinsic rise time and decay time of the scintillator respectively. τ_r = 0.030 ns and τ_d = 40 ns are used to model the intrinsic scintillation of LSO (Derenzo *et al* 2000). I_0 is the mean light yield L or total number of photons generated by the energy deposit. Alternatively, $I(t)$ can be interpreted as the mean photoelectron emission rate function if the quantum efficiency of the photocathode QE_{PMT} (assumed to be constant) is included. In this case, I_0 is the mean photoelectron yield at the photocathode of the PMT. In addition, for a given crystal geometry, the mean number of photons exiting the crystal is less than the total number of photons generated at the excitation point because some photons can be transmitted through the reflecting material (reflection coefficient is not 100%), and some photons are trapped inside the crystal due to internal total reflection on the surface and are eventually absorbed by the bulk crystal or transmitted through the reflecting material. Thus, the light collection efficiency CE_{xtal} is given by the ratio of the mean number of photons exiting the crystal to the total number of photons generated and is included in calculating the mean photoelectron yield I_0.

$$I_0 = L \times QE_{PMT} \times CE_{xtal} \tag{3}$$

The light yield of LSO is taken to be 25,000 photon/MeV (Dorenbos *et al* 1994). We assume QE_{PMT} = 20% (typical for most PMTs and a reasonable number to use for the R-9800 PMT). Thus, $L \times QE_{PMT}$ = 2500 for a 511 keV energy deposit. The factor CE_{xtal} is calculated by simulating the light transport inside the crystal as discussed in Section 2.3.2. In addition, a 511 keV Gaussian energy resolution is modeled by including the contribution from the intrinsic resolution of LSO (5% FWHM of the mean photoelectron yield (Valentine *et al* 1998)) and the photoelectron statistical variation. However, the timing resolution is not dependent on the energy resolution for a symmetrical energy spectrum. In the Monte Carlo timing analysis, we evaluate the dependence of the timing resolution on the scintillator decay times by simulating τ_d = 25, 30, 35, or 40 ns. In addition, in order to study the dependence of the timing resolution on the scintillator light yield, higher values of $L \times QE_{PMT}$ (3000, 4000, and 5000) are also simulated to represent higher light yield scintillators (e.g., $LaBr_3$).

2.3.2. Photon transport inside crystal—The scintillation photon transport inside the crystal is performed using Geant4 (Agostinelli *et al* 2003). The tracking of the individual photons inside the crystal uses the optical processes in Geant4. The UNIFIED model (Levin and Moisan 1996) implemented in Geant4 is employed to simulate the boundary process of scintillation photons between two dielectric media. The UNIFIED model provides a physical model of the surface finish and reflecting material. The model contains seven free parameters as listed in Table 1. The finish is set to "groundbackpainted" to allow the photon to be refracted at the surface and undergo an external diffuse reflection with a probability given by the reflection coefficient RC, which is set to 0.95. n_1 is set to the index refraction of LSO, and n_2 is set to unity to model the reflection material coupling to the surface by air. In the Monte Carlo timing analysis, two type of surface finishes are considered: (a) polished (setting C_{sl} = 1 and $\sigma\alpha$ = 0.1°), and (b) etched (setting C_{sl} = 1 and $\sigma\alpha$ = 6°). Obviously, the distribution of the micro-facet for a polished surface must be small. On the other hand, $\sigma\alpha$ of 6° for an etched surface (Huber *et al* 1999) agrees reasonably well with a measurement by Janecek *et al* 2008.

2.4. Time pick-off methods

2.4.1. First photoelectron timing—The fundamental limit on the timing resolution of a scintillation detector arises from the statistical processes involved in the generation of the photoelectrons, as first discussed by Post and Schiff (1950). For a perfect detector without any SER and transit time spread, this fundamental limit is given by the first photoelectron timing.

In the Monte Carlo analysis, this first photoelectron timing can be determined by looking at the first photoelectron timing spectrum.

2.4.2. Practical timing methods—The timing of the scintillation detector is determined by processing the analog output of the PMT with a time pick-off method. Common to all time pick-off methods, the analog signal is first processed with a front-end voltage amplifier. A practical ultra-wideband, current-feedback operational amplifier (Texas Instruments OPA695) has a bandwidth of 1.4 GHz and an input voltage noise density of 2nV / √Hz. Because the mean PMT signal amplitude is greater than 300 mV in most realizations, a gain of unity is used. Since the analog bandwidth of the fastest SER pulse considered is less than 1.4 GHz, an infinite bandwidth amplifier is modeled in the Monte Carlo analysis. The electronic noise resulting from the practical amplifier is 0.07 mV rms, which is negligible compared to the detector noise of 1–2 mV rms as estimated for the R-9800 PMT by observing the amplitude of the baseline with the oscilloscope. We evaluate the dependence of the timing resolution on the detector noise by adding Gaussian noise of 1, 2, or 3 mV rms to the leading edge of the simulated analog signal.

Three different time pick-off methods are considered: (a) leading edge (LE) discriminator, (b) constant fraction discriminator (CFD), and (c) multi-threshold (MT) discriminator. Figure 7 shows the block diagrams of the LE discriminator and CFD time pick-off methods. The timing jitter in the comparator is negligible because the propagation delay dispersion is less than 30 ps for an ultra-high-speed comparator (Maxim MAX9600). The MT method is implemented using a multiple LE discriminator with different threshold levels. The timing in the MT discriminator is determined by linearly extrapolating the leading edge to the baseline.

2.5. Experimental measurements

Some to the calculated timing resolutions of the simulated scintillation-detector system are compared with experimental measurements. The experimental setup is a coincidence timing measurement similar to the one in measuring the transit time spread of the PMT as discussed in section 2.2. In these measurements a Ge-68 point source is placed between two scintillation detectors to excite them with annihilation gamma rays. A reference trigger signal is generated by coupling a 1 cm cube of BaF_2 to a Hamamatsu H-5321 PMT and is read out with a CFD. This reference detector module has a 150 ps FWHM timing resolution and is used for all measurements. The detector module under test is an LSO crystal coupled to a Hamamatsu R-9800 PMT and is read out with either a CFD or an LE discriminator (Phillips Scientific Model 704). The PMT signal of the test detector module is also amplified by a shaping amplifier, and its amplitude is digitized with an analog-to-digital converter (ADC) to obtain a pulse height spectrum. Only photopeak events defined to be two FWHM wide centered on the photopeak are considered in the timing measurements. To compare with the simulated results, the timing resolution of the test detector module is obtained by subtracting (in quadrature) the measured coincidence timing resolution from the timing resolution of the trigger detector module. We make measurements with different crystal geometries with parameters similar to the simulation. In order to maintain similar light yield in the LSO crystal, we hand-picked crystals that have been cut to 6 mm × 6 mm × 25 mm to have approximately the same photopeak positions in their pulse spectra when excited with 511 keV gamma rays. Half of these crystals are cut to a smaller pixel (4 mm × 4 mm × 25 mm). Then half of the 6 mm × 6 mm × 25 mm and 4 mm × 4 mm × 25 mm crystals are polished and the other half are chemically etched (Huber *et al* 1999). The crystals are wrapped with four layers of Teflon. To minimize statistical error, we perform the measurements with four different crystals, each with the same pixel size and surface finish. The measurements are performed starting with the crystals at their longest length and cutting them to shorter lengths (10, 15, 20 mm), which reduce crystal-to-crystal variations.

3. Results

3.1. Dependence of timing on the photoelectron yield and scintillator decay time

Figure 8 shows the timing resolution as a function of the mean photoelectron yield I_0 for different scintillator decay time constants. Two plots are shown in Figure 8, one for a short crystal (10 mm) and the other for a long crystal (25 mm). Each plot shows the calculated timing resolution using the first photoelectron timing and CFD timing. As expected, the timing resolution improves with increasing photoelectron yield and faster scintillator decay time constant. The CFD timing correlates inversely proportional to the square root of the mean photoelectron yield (Hyman 1965 and Tomitani 1982) and proportional to the square root of the scintillator decay time constant reasonably well with an error of less than 4%. On the other hand, the first photoelectron timing follows a different power law as shown in Figure 8, which is consistent with the theory by Post and Schiff 1950.

3.2. Dependence of timing on the time pick-off method

Figure 9 shows the timing resolution as a function of the CFD delay for different CFD fractions. Two sets of data are presented in the plot representing two mean photoelectron yields. The best timing resolution is obtained with a CFD fraction of 15%. At this fraction the timing resolution does not vary significantly with the CFD delay. Interestingly, the timing resolution converges to an optimum value with a small CFD delay at 0.5 ns independent of the CFD fraction. Below a CFD delay of 0.5 ns, the zero-crossing slope decreases significantly, resulting in large CFD timing jitter (not shown in the plot).

Figure 10 shows the timing resolution as a function of the LE threshold for two different crystal surface finishes. Two plots are shown in Figure 10, one for a short crystal (10 mm) and the other for a long crystal (25 mm). Also shown on each plot are the best CFD timing and the first photoelectron timing. The shape of the curves is similar to that reported by others (Hyman 1965). Because of the amplitude walk, the timing resolution degrades with increasing LE threshold. A minimum timing resolution is achieved as the curve turns up at low LE thresholds due to the TTS of the SER (Hyman 1965). The LE discriminator performs better than the CFD when an optimum LE threshold is used.

The timing resolution using the MT discriminator is listed in Table 2. The results using one, two, and three threshold levels are reported. For the two- and three-threshold discriminator, different combinations of the thresholds sampling the leading edge of the signal are evaluated. The best MT timing (up to three threshold levels) is comparable to the best LE timing.

Since the LE timing gives the best timing resolution among the three time pick-off methods, we therefore focus our Monte Carlo analysis on the LE timing in the remainder of this work.

3.3. Dependence of timing on the noise

Figure 11 shows the timing resolution as a function of the LE discriminator threshold for different noise levels. The best timing degrades slightly by less than 4% for noise levels between 0 to 2 mV rms as compared to a noiseless detector. Because the time jitter arising from the random noise is inversely proportional to the slope of the leading edge of the signal, the small degradation may be due to the fact that the rise time of simulated signal is fairly fast (< 1 ns for the R9800 PMT). However, above 2 mV rms noise level, the timing degrades significantly as the noise approaches the level of the threshold. As mentioned previously, the detector noise of the R-9800 PMT is 1–2 mV rms, which is typical of other PMTs as well. Thus, the timing jitter introduced by the noise can be considered negligible.

3.4. Dependence of timing on the TTS and SER pulse width

Figure 12 shows the timing resolution as a function of the LE discriminator threshold for different TTS values. The SER pulse width is 1.18 ns FWHM. Two plots are shown in Figure 12, one for a short crystal (10 mm) and the other for a long crystal (25 mm). As expected, the timing resolution improves with decreasing TTS. The best timing resolution is obtained at a low optimum LE threshold. For low enough TTS (TTS close to or below the first photoelectron timing), the best timing is obtained at the lowest LE threshold. This behavior is consistent with the Hyman theory (Hyman 1965). A decrease in the TTS from 300 ps to 100 ps improves the timing resolution from 184 ps to 143 ps for the short crystal (22% improvement) and from 207 ps to 172 ps for the long crystal (17% improvement). While there are further timing improvement that can be obtained for the short crystal if lower TTS is used, the timing resolution for the long crystal is already close to the first photoelectron timing for TTS=100 ps.

Similar plots are shown in Figure 13 for an SER pulse width of 0.31 ns FWHM. The best timing resolution is comparable to the longer SER pulse width in Figure 12 for TTS=100 ps FWHM. However, for low TTS values the best timing resolution can be obtained with a higher LE threshold rather than at the lowest threshold in the longer SER pulse width. Note that the mean amplitude of signal is smaller because faster SER pulse width leads to less superposition of the SER pulses from the photoelectron emission. This smaller amplitude may contribute to the timing degradation observed for large TTS values in Figure 13.

3.5. Dependence of timing on the crystal properties

Figure 14 shows the timing resolution as a function of the crystal length. The timing resolution is calculated using an LE discriminator (the threshold is set at 10 mV) and a CFD (fraction of 20% and a delay of 0.5 ns). Two plots are shown in Figure 14, one for a short crystal (10 mm) and the other for a long crystal (25 mm). Each plot presents the results for two different crystal surface finishes and two pixel sizes. As expected, the timing degrades with increasing length. In addition, the timing resolution for an etched crystal is better than for a polished crystal. These results can be explained by looking at the initial photoelectron rate, which can be defined as the total photoelectron generated for a specific time interval on the leading part of the photoelectron rate curve, as shown in Figure 15. Statistically, a higher initial photoelectron rate gives better timing resolution. As shown in Figure 15, a 10 mm long crystal has higher initial photoelectron rate than a 25 mm crystal, and an etched crystal has higher initial photoelectron rate than a polished crystal. Further observations of the photoelectron rate suggest that the initial rate is higher for the etched crystal with a larger pixel size, but the difference becomes relatively small for the long crystal. On the other hand, the initial rate is very similar for the polished crystal independent of pixel sizes. These two observations in the initial photoelectron rate are reflected in the calculated timing resolution as shown in Figure 14. Furthermore, the leading part of the simulated photoelectron rate is similar for polished and etched crystals. Thus, the first photoelectron timing is expected to be similar for polished and etched crystals and is confirmed in Figure 10.

3.6. Comparison of experimental measurement and Monte Carlo calculation

The calculated timing resolutions are compared with experimental measurements. Figure 16 shows the measured timing resolution as a function of LE discriminator threshold level for a short crystal (6 mm × 6 mm × 10 mm) and a long crystal (6 mm × 6 mm × 25 mm). The timing resolutions are also measured with a CFD. The data show a similar response as the calculated results in Figure 10. The measured timing resolution achieves a minimum value at an optimum low LE threshold. The timing resolution for an etched crystal is better than a polished crystal. Furthermore, the LE timing performs better than the CFD timing confirming the Monte Carlo results. While there are some discrepancies in a few of the measured timing resolutions

compared to the calculated values, in general they are in good agreement. One discrepancy is that the measured CFD timing resolution of the short etched crystal (192 ps) is slightly lower than the calculated value (215 ps). Another discrepancy is that the measured LE timing resolutions of the long crystals are 11–15% higher than the calculated values, but the CFD timing resolutions are in good agreement.

Figure 17 shows the measured timing resolution as a function of crystal length for two crystal surface finishes (polished and etched) and two pixel sizes (4 mm × 4 mm and 6 mm × 6 mm). For the small pixel size, only etched crystals are measured. The timing resolutions are measured using a CFD. The measured timing resolution degrades with increasing crystal length, which is consistent with the calculated results in Figure 14. The measured timing resolution of the etched crystal exhibits very little dependence on the pixel sizes. In general, the measured timing resolution of the etched crystal is better than the polished crystal. However, similar performance is obtained for crystal lengths greater than 20 mm independent of surface finishes or pixel sizes. Although the measured timing resolutions are comparable to the calculated results in Figure 14, they are not in complete agreement for short crystal lengths (less than 20 mm). The measured timing resolutions for short crystal lengths are better than the calculated values, especially for etched crystals.

4. Discussion and conclusion

A number of results are obtained from our Monte Carlo analysis: (1) the CFD timing resolution is inversely proportional to the square root of a rate defined by the ratio of the photoelectron yield to the scintillator decay time constant I_0 / τ_d; (2) the LE discriminator gives better timing than the CFD or the MT discriminator; (3) the timing resolution shows negligible dependence on noise less than 2 mV rms; (4) the timing resolution improves with decreasing TTS and substantial improvement is obtained if the first photoelectron timing is less than the TTS; (5) while the timing resolution does not improve with a fast SER pulse width, the best timing resolution can be obtained with a higher LE threshold; (6) the timing resolution degrades with increasing crystal length; (7) etched crystal has better timing resolution than polished crystal; and (8) while a 4 mm × 4 mm pixel has a slightly better timing resolution than a 6 mm × 6 mm pixel, the difference becomes negligible for long or polished crystals. Some of the Monte Carlo results are confirming common knowledge of timing of scintillation detectors. However, a few important and interesting results, which have not been previously studied extensively, emerges from the analysis that relate to how the timing depends on the TTS, SER, and the time pick-off method. In addition, the dependence of timing on crystal properties can be explained by studying the initial the photoelectron rate.

Figure 12 and 13 suggest that a substantial gain in the timing resolution can be obtained by improving the TTS if the first photoelectron timing is substantially less than the TTS. On the other hand, the gain in timing resolution would be small by improving the TTS if the first photoelectron timing is greater than the TTS because the timing resolution is limited by the photoelectron statistics. With low enough TTS, the best timing resolution approaches the first photoelectron timing at a low LE threshold because triggering at low LE threshold is equivalent to picking off the timing of the first few photoelectrons. If the LE threshold is low enough, the timing is the first photoelectron timing if the individual photoelectron can be distinguished as in the case of low TTS and fast SER. Thus, in order to yield substantial improvement in the timing resolution from a photodetector with low TTS, the first photoelectron timing must be less than the TTS. There are a few approaches to improve the first photoelectron timing, which include using scintillator materials with high light yield and fast decay time (e.g. LSO, $LaBr_3$, LuI_3), photodetector with high particle detection efficiency (e.g. super bialkali photocathode or ultra bialkali photocathode), and short crystals (less than 20 mm). A photodetector with excellent TTS is an MCP PMT. Depending on the pore size of the MCP,

the TTS for an MCP can be less than 100 ps FWHM (Va'vra *et al* 2007). In addition, an MCP PMT can be fabricated with a large active area and a multiple anode readout, which is suitable for a TOFPET detector module.

Because of the amplitude walk, it is a common practice to use the CFD to obtain the optimum timing performance. However, our analysis shows that the LE discriminator performs better than the CFD when an optimum LE threshold is used, which is a small fraction (less than 10%) of the average amplitude of the photopeak signal. This interesting result is validated by experimental measurements. While CFD is used to trigger at a fixed fraction (10–20%) of the pulse amplitude, it does not give the first photoelectron timing because of the high threshold. In addition, the first photoelectron timing can be achieved with a photodetector having a low TTS and a very fast SER. In this case, a short CFD delay would yield the optimum timing for fast SER, but would also reduce the zero-crossing slope resulting in increased CFD timing jitter. On the other hand, as discussed above, the LE discriminator timing can potentially approach the first photoelectron timing. A consequence of this result is that the front-end electronics can be simplified by implementing an LE discriminator rather than a CFD.

Some of the calculated timing resolutions from our Monte Carlo analysis are compared with experimental measurements. While the calculated and measured timing resolution agrees reasonably well in some cases, there are some discrepancies. The discrepancies appear more pronounced for short etched crystals, which may be due to several factors. First, the estimated photoelectron yield used in the Monte Carlo analysis could be different from the actual photoelectron yield in the measurements. Second, the parameters used in the UNIFIED model to simulate the etched crystals might not be completely accurate. Third, in the measurements, the crystals are cut from their longest length at 25 mm to shorter lengths. However, there are some difficulties in controlling the accuracy of the cut, and thus in some crystals the length could differ by as much as 1 mm.

In summary, we have developed a Monte Carlo analysis that will allow the optimization of the timing performance in scintillation-detector systems. More importantly, it will also help us to understand the physical processes that limit the timing performance. In this work, we have studied how the scintillator response, photodetector response, and different time pick-off methods affect the timing resolution. The calculated timing resolution can be useful in predicting the performance gain in a TOF PET camera.

Acknowledgments

The author would like to thank W. W. Moses for many useful discussions and his interest in this work. This work was supported in part by the Director, Office of Science, Office of Biological and Environmental Research, Medical Science Division of the U.S. Department of Energy under Contract No. DE-AC02-05CH11231, and in part by the National Institutes of Health, National Institute of Biomedical Imaging and Bioengineering under grant No. R21EB007081 and R01EB006085.

References

Agostinelli S, et al. Geant4–a simulation toolkit. Nucl. Instrum. Methods A 2003;506:250–303.

Bengtson B, Moszynski M. Timing properties of scintillation counters. Nucl. Instrum. Methods 1970;81:109–20.

Binkley DM. Optimization of scintillation-detector timing systems using Monte Carlo analysis. IEEE Trans. Nucl. Sci 1994;41:386–93.

Campagnolo, RE.; Garderet, P.; Vacher, J. Communication an Colloque National sur le Traitement du Signal. Nice; France: 1979. Tomographic par emeterurs positrons avec mesure de temp de vol.

Clinthorne NH, Petrick HA, Rogers WL, Hero AO III. A fundamental limit on timing performance with scintillation detectors. IEEE Trans. Nucl. Sci 1990;37:658–63.

Conti M. Effect of randoms on signal-to-noise ratio in TOF PET. IEEE Trans. Nucl. Sci 2006;53:1188–93.

Derenzo SE, Weber MJ, Moses WW, Dujardin C. Measurements of the intrinsic rise time of common inorganic scintillators. IEEE Trans. Nucl. Sci 2000;47:860–4.

Dorenbos P, de Haas JTM, van Eijk CWE, Melcher CL, Schweitzer JS. Non-linear response in the scintillation yield of $Lu_2SiO_5:Ce^{3+}$*. IEEE Trans. Nucl. Sci 1994;41:735–7.

Harrison, RL.; Alessio, AM.; Kinahan, PE.; Lewellen, TK. Signal to noise ratio in simulations of time-of-flight positron emission tomography; Proc. IEEE Nuclear Science Symposium and Medical Imaging Conference; 2004; p. 4080-3.

Huber JS, Moses WW, Andreaco MS, Loope M, Melcher CL, Nutt R. Geometry and surface treatment dependence of the light collection from LSO crystals. Nucl. Instrum. Methods A 1999;437:374–80.

Hyman LG. Time resolution of photomultiplier systems. Rev. Sci. Instr 1965;36:193–6.

Janecek M, Moses WW. Measuring light reflectance of BGO crystal surfaces. IEEE Trans. Nucl. Sci 2008;55:2443–9.

Levin, A.; Moisan, C. A more physical approach to model the surface treatment of scintillation counters and its implementation into DETECT; IEEE Nucl. Sci. Symposium Conference Record; 1996; p. 702-6.

Knoll, GF. Radiation Detection and Measurement. third edition. John Wiley & Sons, Inc.; New York: 2000.

Lynch FJ. Improved timing with NaI(Tl). IEEE Trans. Nucl. Sci 1966;33:140–7.

Muehllehner G, Karp JS. Positron emission tomography. Phys. Med. Biol 2006;51:R117–R137. [PubMed: 16790899]

Surti S, Karp JS, Popescu LM, Daube-Witherspoon ME, Werner M. Investigation of time-of-flight benefit for fully 3-D PET. IEEE Trans. Med. Imaging 2006;25:529–38. [PubMed: 16689258]

Synder DL, Thomas LJ, Ter-Pogossian MM. A mathematical model for positron-emission tomography systems having time-of-flight measurements. IEEE Trans. Nucl. Sci 1981;28:3575–83.

Post RF, Schiff LI. Statistical limitation on the resolving time of a scintillation counter. Phy. Rev 1950;80:1113.

Melcher CL, Schweitzer JS. Cerium-doped lutetium oxyorthosilicate – a fast, efficient new scintillator. IEEE Trans. Nucl. Sci 1992;39:502–5.

Moses WW. Time of flight in PET revisited. IEEE Trans. Nucl. Sci 2003;50:1325–30.

Tomitani T. Image reconstruction and noise evaluation in photon time-of-flight assisted positron emission tomography. IEEE Trans. Nucl. Sci 1981;28:4582–89.

Tomitani, T. A maximum likelihood approach to timing in scintillation counters; Proceedings of the IEEE Workshop on Time-of-Flight Tomography; 1982; p. 88-93.

Valentine JD, Rooney BD, Li J. The light yield nonproportionality component of scintillator energy resolution. IEEE Trans. Nucl. Sci 1998;45:512–7.

van Loef EVD, Dorenbos P, van Eijk CWE, Kramer KW, Gudel HU. Scintillation properties of $LaBr_3:Ce^{3+}$ crystals: fast, efficient and high-energy-resolution scintillators. Nucl. Instrum. Methods A 2002;486:254–8.

Va'vra J, Benitez J, Leith DWGS, Mazaheri G, Ratcliff B, Schwiening JA. A 30 ps timing resolution for single photons with multi-pixel Burle MCP-PMT. Nucl. Instrum. Methods A 2007;572:459–62.

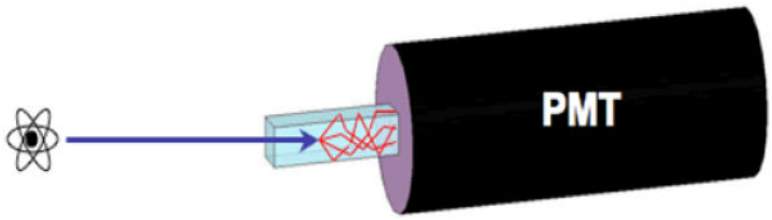

Figure 1.
Schematic diagram of a scintillation detector modeled by the Monte Carlo simulation.

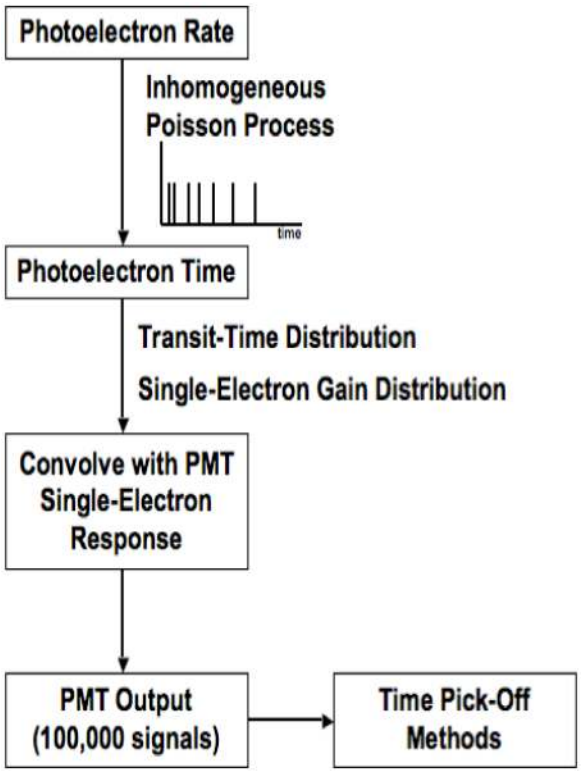

Figure 2.
Block diagram of Monte Carlo timing analysis.

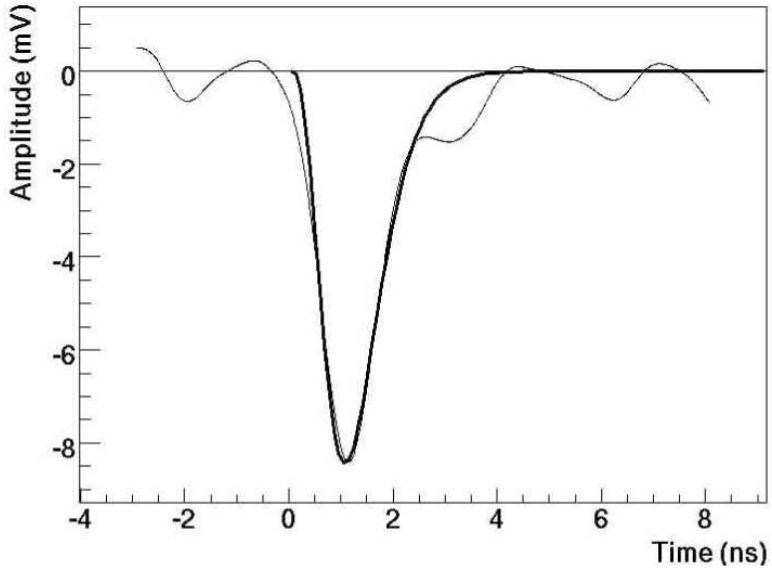

Figure 3.
Measured mean SER of R-9800 PMT modeled by a truncated Gaussian function.

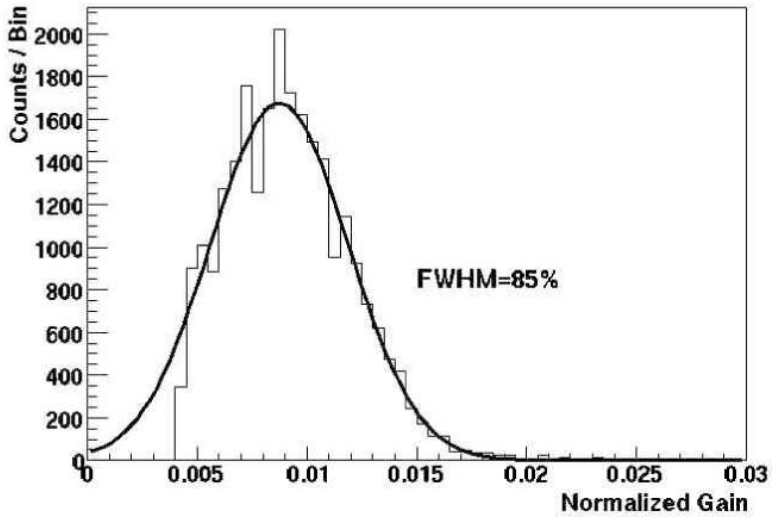

Figure 4.
Measured SER gain distribution of R-9800 PMT modeled by a Gaussian function.

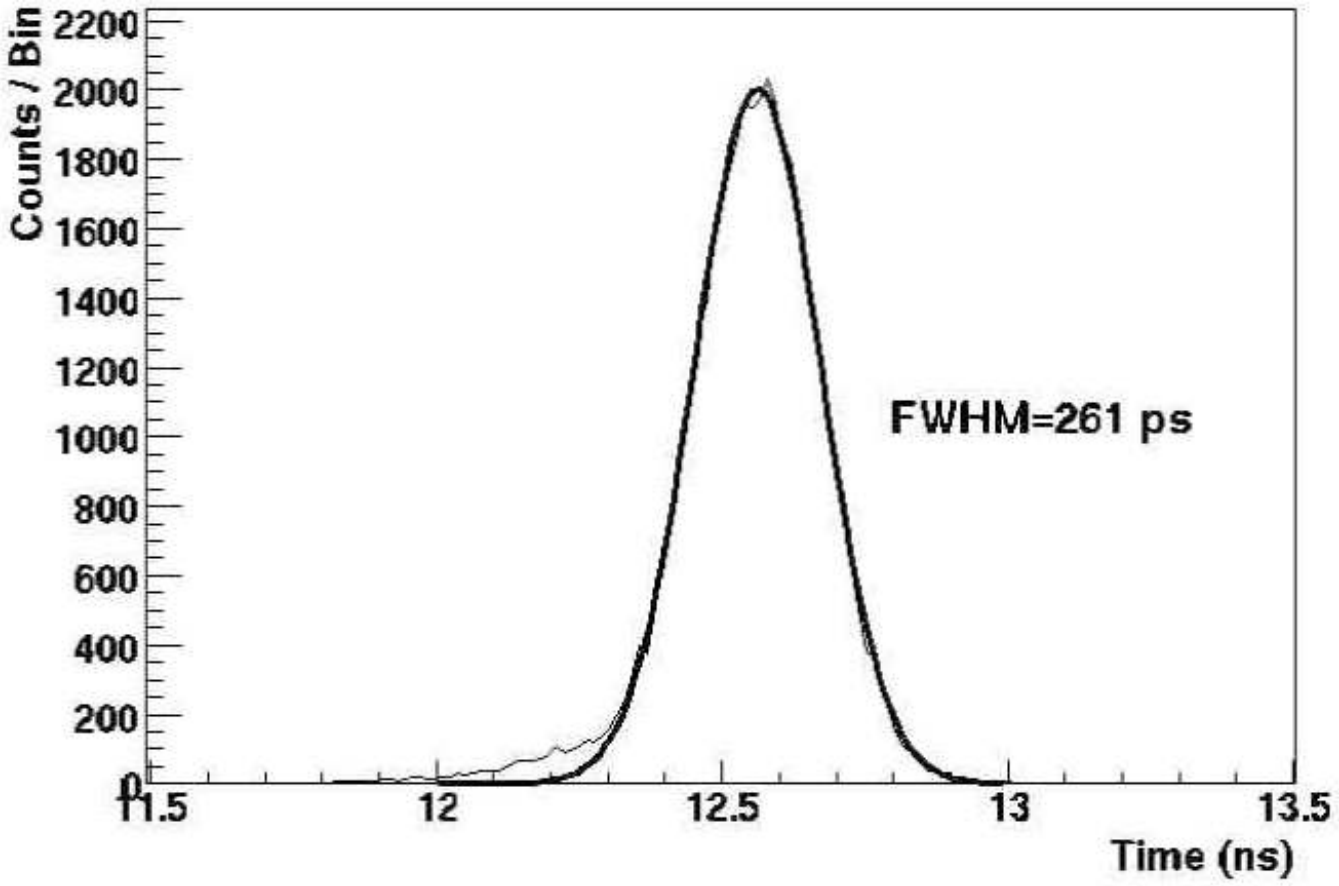

Figure 5.
Measured transit time spectrum of R-9800 PMT modeled by a Gaussian function.

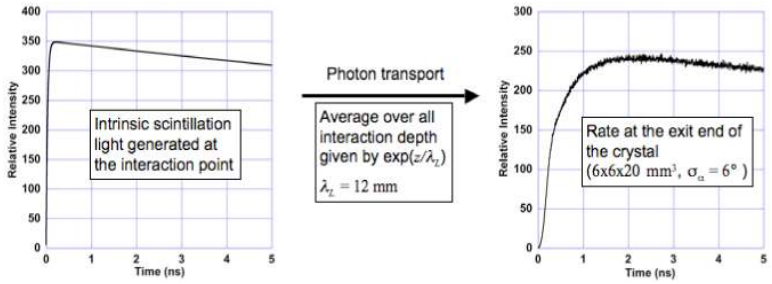

Figure 6.
Simulated photoelectron rate function for a 6×6×20 mm^3 LSO crystal.

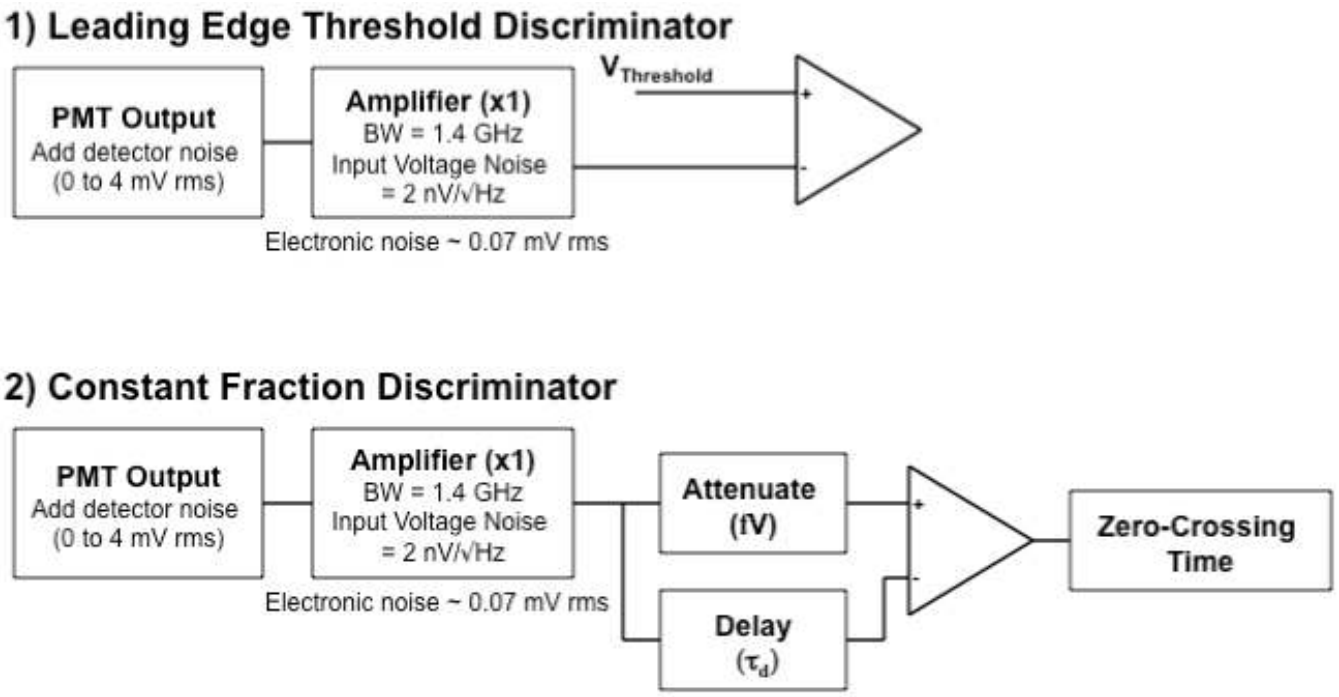

Figure 7.

Block diagram of LE and CF discriminator time pick-off methods. The bandwidth of the amplifier is assumed to be infinite in the Monte Carlo analysis because the analog bandwidth of the fastest SER pulse considered is less than 1.4 GHz.

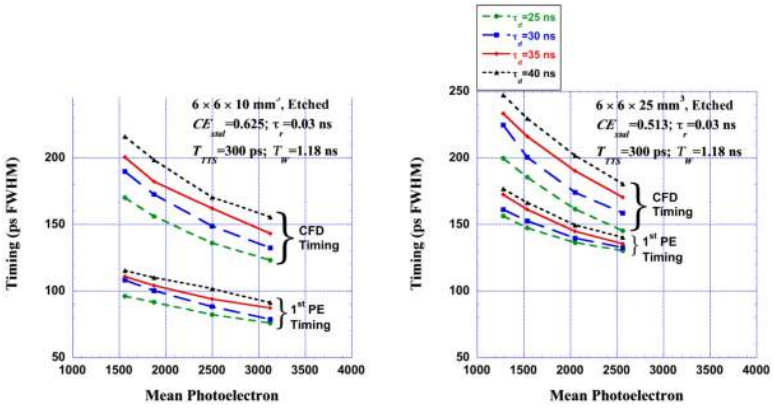

Figure 8.

Timing resolution as a function of the mean photoelectron yield for τ_{decay}= 25, 30, 35, and 40 ns. The first photoelectron timing and CFD timing is calculated for a short crystal (left) and a long crystal (right).

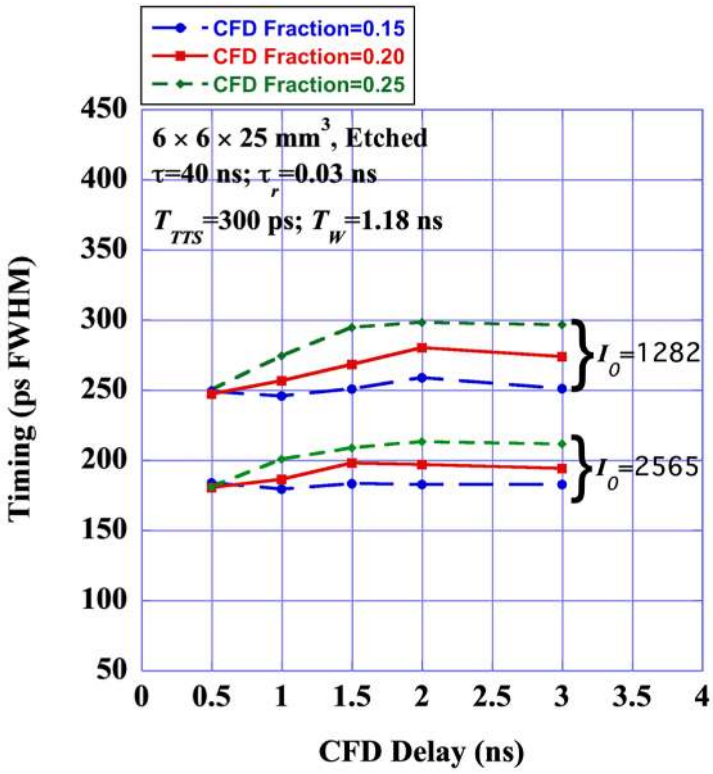

Figure 9.
Timing resolution as a function of the CFD delay for three CFD fractions and two mean photoelectron yields.

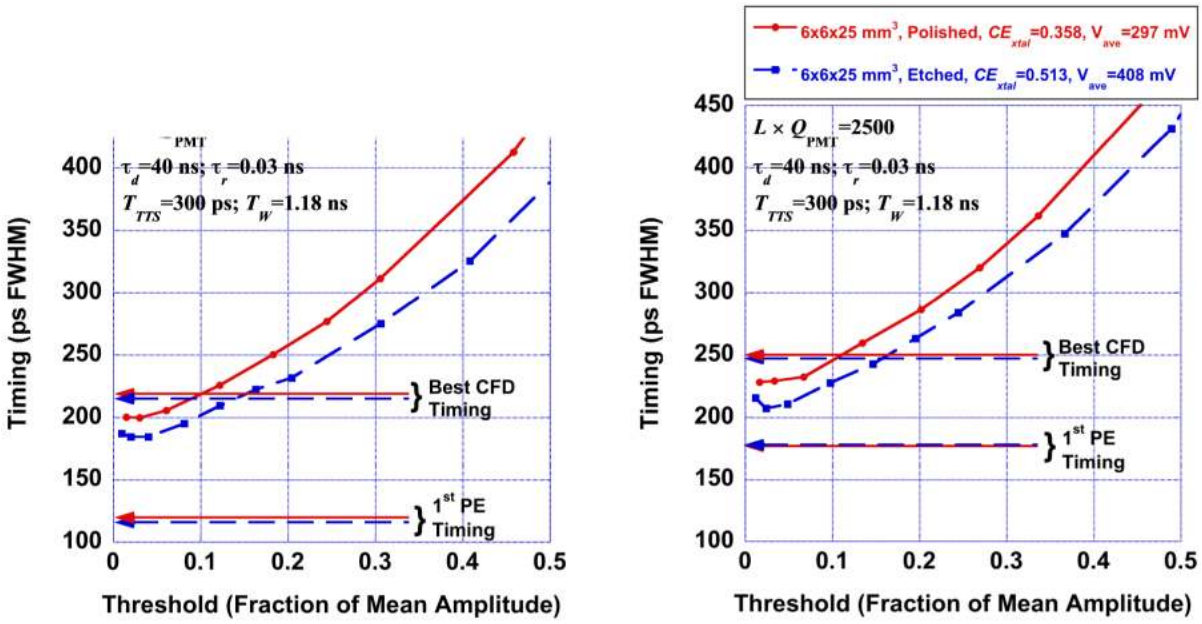

Figure 10.

Timing resolution as a function of the LE discriminator threshold for polished and etched crystals. The timing resolution is calculated for a short (left) and a long (right) crystal. The first photoelectron timing and best CFD timing are also shown in the plots for comparison.

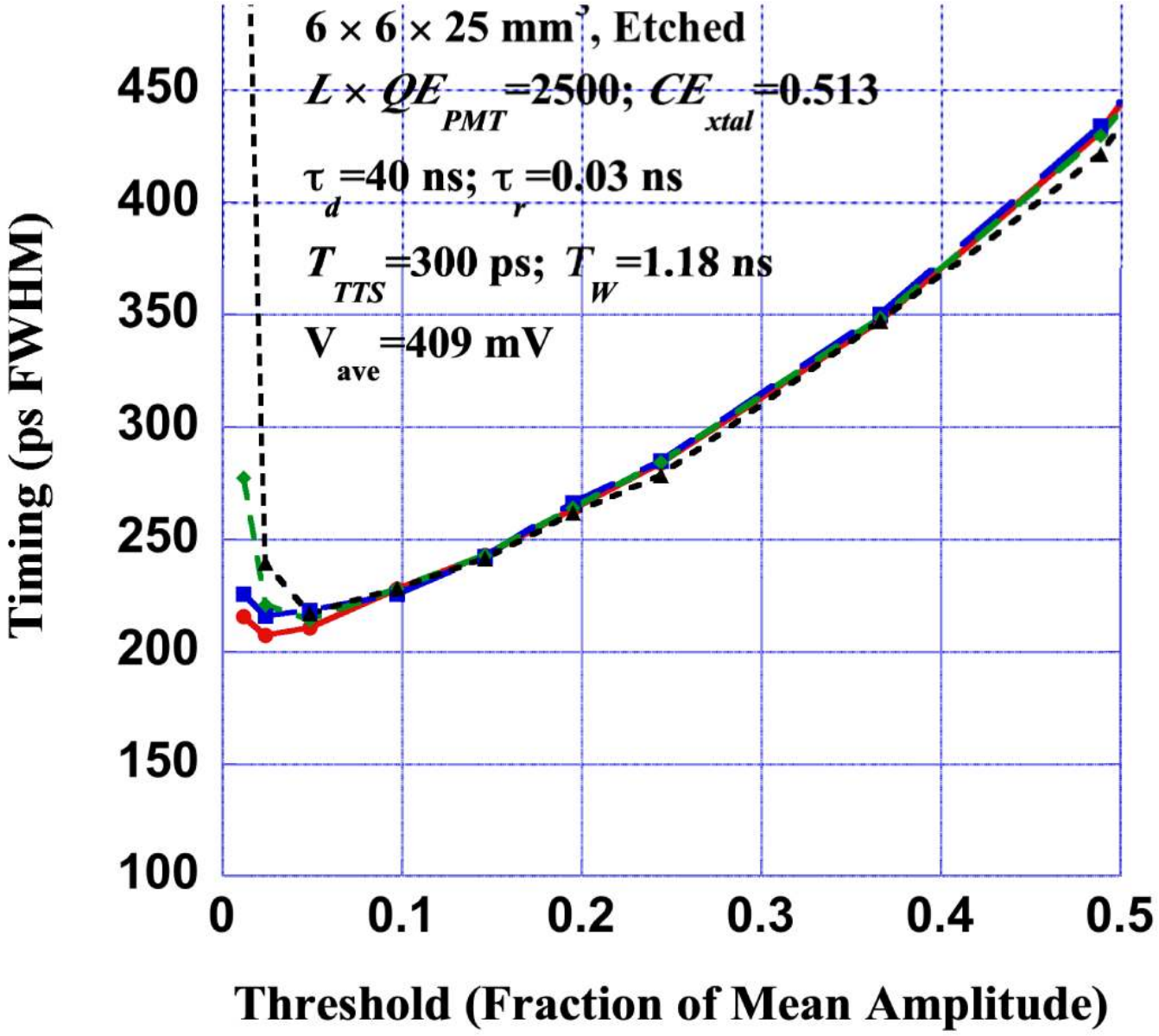

Figure 11.
Timing resolution as a function of the LE discriminator threshold for noise levels equal to 0, 1, 2, and 3 mV rms.

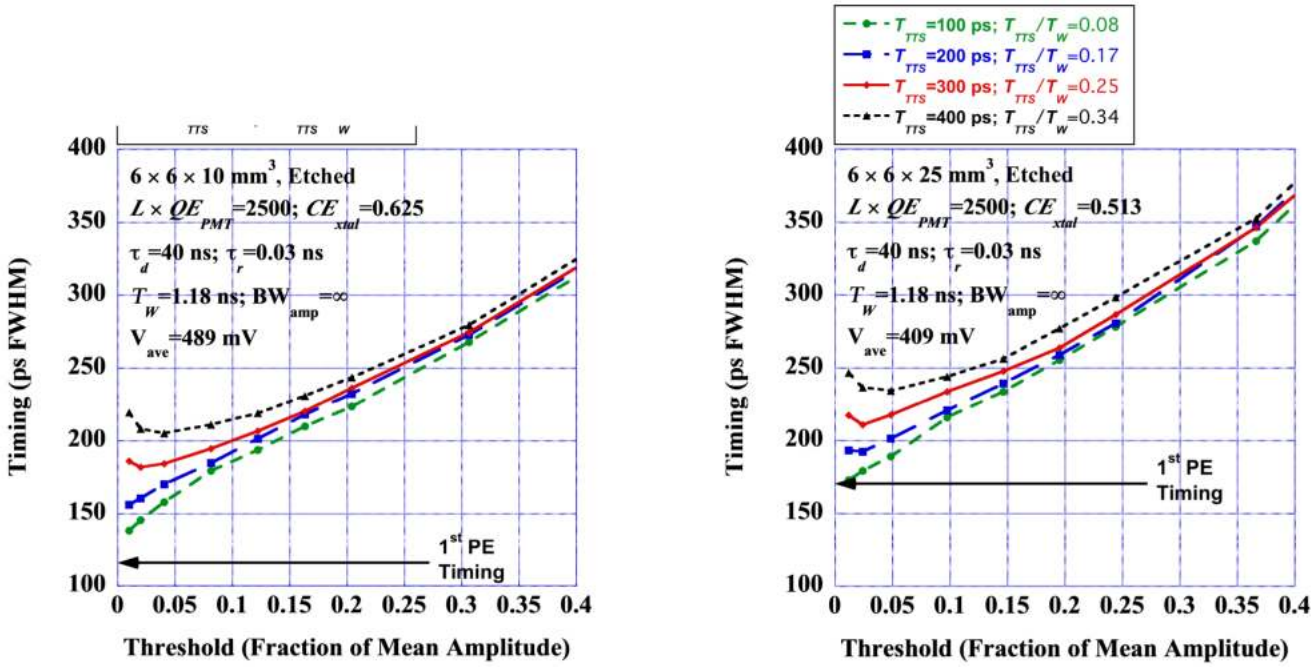

Figure 12.
Timing resolution as a function of the LE discriminator threshold for transit time spread T_{TTS} = 100, 200, 300, and 400 ps FWHM. The SER pulse width is 1.18 ns FWHM. The timing resolution is calculated for a short (left) and a long (right) crystal. The first photoelectron timing is also shown in the plots.

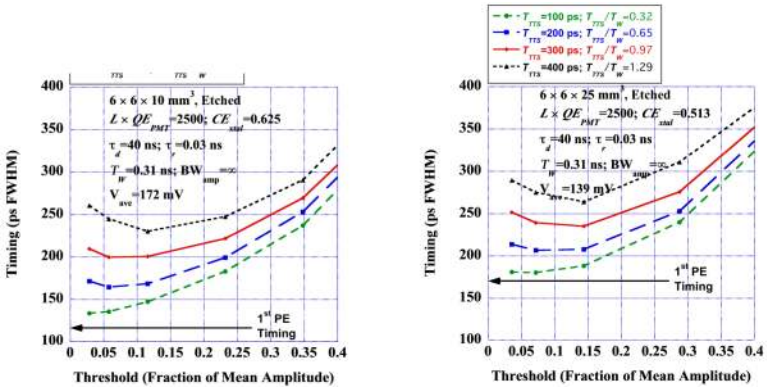

Figure 13.

Timing resolution as a function of the LE discriminator threshold for transit time spread T_{TTS} = 100, 200, 300, and 400 ps FWHM. The SER pulse width is 0.31 ns FWHM. The timing resolution is calculated for a short (left) and a long (right) crystal. The first photoelectron timing is also shown in the plots.

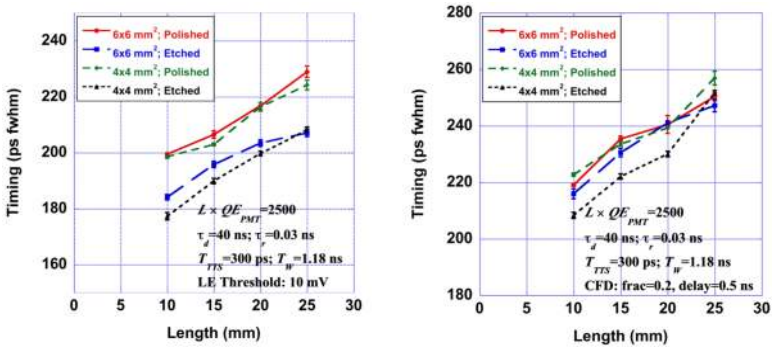

Figure 14.

Timing resolution as a function of the crystal length for polished and etched crystals with pixel sizes 4 mm × 4 mm and 6 mm × 6 mm. The timing resolution is calculated using an LE discriminator (left) and a CFD (right).

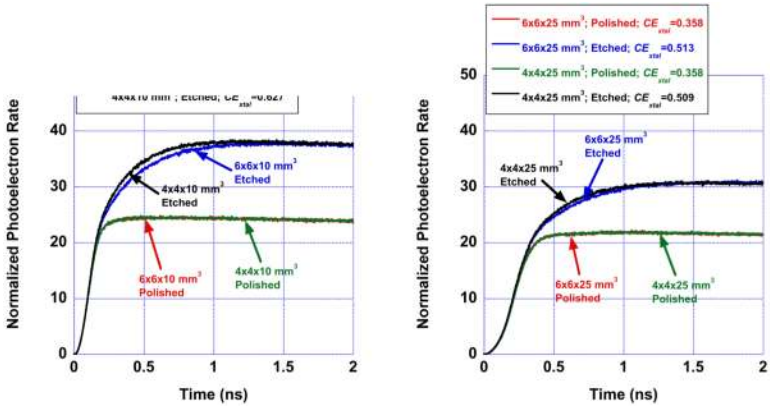

Figure 15.

Simulated photoelectron rate as a function of time. The curves are normalized such that the total area under the curve is equal to the mean photoelectron yield for that particular crystal with $L \times QE_{PMT} = 2500$. The timing resolution is calculated for a short (left) and a long (right) crystal.

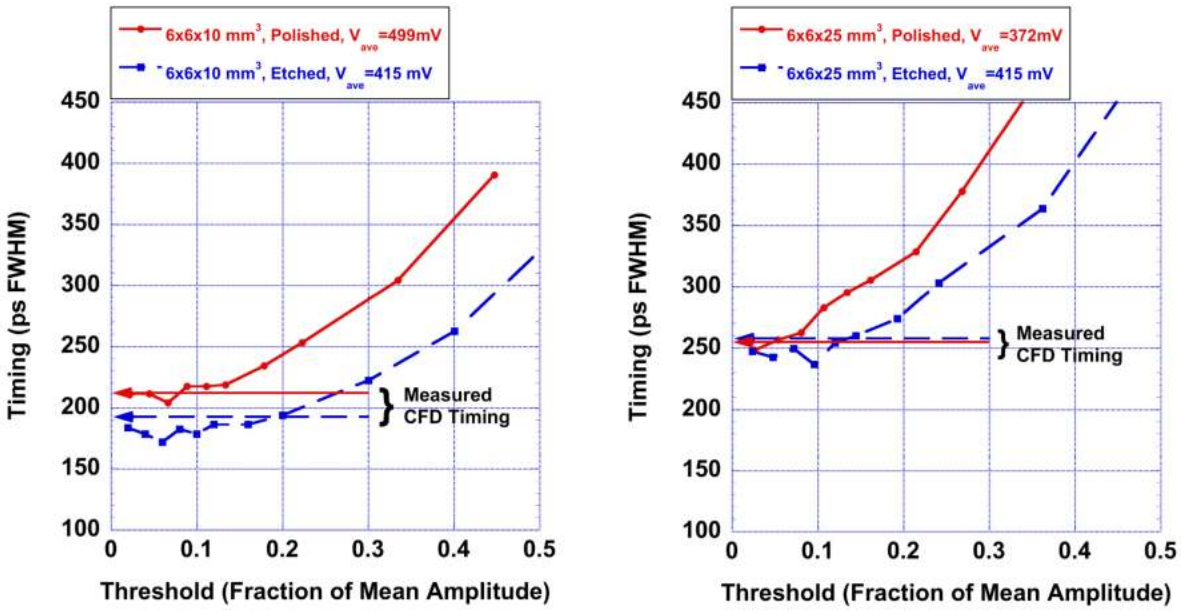

Figure 16.
Measured timing resolution as a function of the LE discriminator threshold for polished and etched crystals. The timing resolution is measured for a short (left) and a long (right) crystal. The measurement is also performed with CFD timing for comparison.

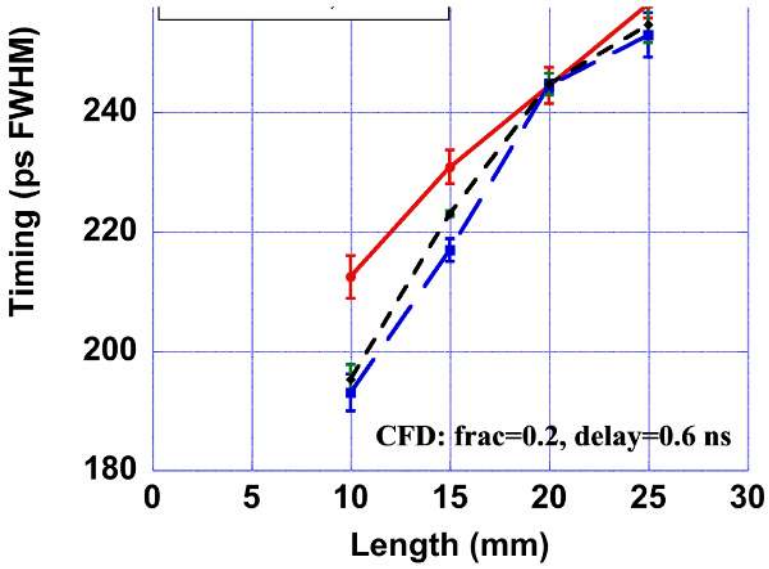

Figure 17.
Measured timing resolution as a function of the crystal length. The timing resolution is measured using a CFD.

Table 1

Parameters in UNIFIED model

Parameter	Description
n_1	index reflection of the incident medium
n_2	index reflection of the transmission medium
RC	reflection coefficient
σ_α	standard deviation of the angle between the micro-facet normal and the average surface normal α
C_{sl}	probability of specular reflection about the normal of a microfacet
C_{ss}	probability of specular reflection about the average normal of the surface
C_{bs}	probability of backward reflection
C_{dl}	probability of internal diffuse reflection

Note: $C_{sl} + C_{ss} + C_{bs} + C_{dl} = 1$

Table 2

Timing resolution of multi-threshold discrimination

1-Threshold (Fraction of Mean Amplitude)	Timing (ps FWHM)	2-Threshold (Fraction of Mean Amplitude)	Timing (ps FWHM)	3-Threshold (Fraction of Mean Amplitude)	Timing (ps FWHM)
0.012	215	0.024, 0.098	213	0.024, 0.049, 0.098	210
0.024	207	0.024, 0.15	211	0.024, 0.049, 0.15	211
0.049	210	0.024, 0.24	210	0.024, 0.098, 0.20	211
0.098	227	0.024, 0.37	209	0.024, 0.20, 0.37	210
0.15	243	0.024, 0.49	211	0.024, 0.24, 0.61	222
0.20	263	0.15, 0.24	234		
0.24	284	0.15, 0.37	244		